2017

A Multiscale Model for Damage Progression and Detection in Piezo/Pyroelectric Composite Laminates

Yehia Bahei-El-Din
ybahei@bue.edu.eg

Amany Micheal
The British University in Egypt, amany.michael@bue.edu.eg

A Multiscale Model for Damage Progression and Detection in Piezo/Pyroelectric Composite Laminates

Yehia A. Bahei-El-Din and Amany Micheal

Center for Advanced Materials
The British University in Egypt
El-Shorouk City, Egypt

ABSTRACT

Assessment of damage initiation and progression in composite structures reinforced with electrically active filaments is modelled in a multiscale analysis. The analysis developed is a two-tier, interactive analysis, which involves two length scales; macroscopic, and microscopic. The proposed multiscale analysis provides seamless integration of the mechanics at the two length scales, including piezoelectric and pyroelectric coupling effects and damage under overall thermomechanical loads and an electric field applied to electroactive fibers. The macromechanical analysis is performed for multidirectional, fibrous laminates using the lamination theory, including bending, and the micromechanical analysis is performed using a two-phase model and a periodic array model. The effect of eigenstrains caused by thermomechanical, electromechanical, and thermoelectric coupling at both the microscopic and macroscopic length scales is accounted for by a two-tier transformation field analysis (TFA).

KEYWORDS

Multifunctional composites, Laminates, Plates, Thermomechanical, Computational modelling, Damage mechanics, Laminate mechanics, Micro-mechanics.

1. INTRODUCTION

Piezoelectric materials have been used as both sensors and actuators for smart structures. They may be used for structural health monitoring (SHM) or for control of deformation purposes. In applications where this functionality together with a decent load carrying capacity are desired, piezoelectric filaments are embedded in a polymeric matrix to form an electroactive unidirectional composite, which may be utilized in various laminated or woven architectures. Research in electrically active composites has seen both modeling and experimental efforts. In one class of work, which is relevant to that presented here, the focus has been on prediction of the overall properties of piezoelectric composites, including mechanical, electrical and coupled effects, particularly within the micromechanics framework. This is found for example in the work of Aboudi [1], Berger et al. [2], Challagulla and Georgiades [3], Chen [4], Hadjiloizi et al. [5, 6], Della and Shu [7], and Kumar and Chakraborty [8] among others.

Multiscale models on the other hand were limited to inactive composites but included damage. This is found in the two-scale models of Sato et al. [9] for crack initiation in cross ply laminates and Ivančević and Smojver [10] for microscale damage. The latter combined finite elements of a unit cell of the microstructure and homogenization to model the effect of local damage on overall properties. Spahn et al. [11] on the other hand combined finite elements and analytical modeling using integral equations and fast Fourier transformation to capture the effect of localized damage on the overall response of fibrous composites, while Liu et al. [12] combined continuum damage, micromechanics and finite elements to predict failure of composite pressure vessels. A macro/meso model, which utilized a hexagonal representative volume element of fibrous composites was developed by Li et al. [13] to model damage caused by thermomechanical loads, and global-local numerical strategies which couple a mesoscale,

continuum model and microscale models can be found in the work of Daghia and Ladevèze [14, 15] , Kurnatowski and Matzenmiller [16], Mao et al. [17], and Zhang et al. [18]. Two-scale models for damage in composite laminates based on transformation field analysis can be found in the work of Bahei-El-Din and Botrous [19] for fiber debonding, Bahei-El-Din et al. [20] for macroscopic failure of plies, and Khire et al. [21] for uncertainties associated with propagation of damage. A recent comparison of various models with experiments is found in Kaddour and Hinton [22, 23]. Multiscale modeling of composites including damage can be also found for particulate composites [24-26], and for woven composites [27-31].

Modeling of fibrous composites with electroactive fibers using multiscale models can be found in the work of Bahei-El-Din and Micheal [32, 33] for undamaged fibrous laminates and fibrous laminated structures, respectively. The only treatment of damage in composites reinforced with piezoelectric fibers can be found in the work of Bahei-El-Din [34] for 3D woven composites. In this work, multiscale modeling was performed with a transformation field analysis and relied on the periodic construction of the 3D woven architecture to find a unit cell which is representative of the overall behavior. In this case, the unit cell is subdivided into small volumes over which the local stress distribution is modeled as piecewise uniform. Extension of this approach to fibrous laminates of a general layup is not possible since a unit cell can be found for very limited layups, e.g. cross plies.

To offer a multiscale solution for the overall behavior of piezoelectric composite laminates with a general layup, which incorporates damage, the present paper combines lamination theory and micromechanical models of fibrous composites in a two tier, thermo-electro-mechanical transformation field analysis (TFA) approach. Laminate geometry, loads and materials are described in Section 2 and constitutive equations and interrelations for fibrous composites

microscale and laminate macroscale are detailed in Section 3. In Section 4, transformation fields caused in multidirectional laminates by thermos-electro-mechanical coupling of piezoelectric filaments and damage are examined. Utilizing the proposed methodology in monitoring deformations within fibrous laminates is presented in Section 5, with several applications given in Section 6, and comparison with experimental measurements given in Section 7. The paper closes with conclusions and future work in Section 8.

2. GEOMETRY, MATERIALS AND LOADS

The problem under consideration is that of piezoelectric fibrous laminates subjected to thermomechanical loads as well as internal deformations which may result from local electric fields and/or electric displacements. The laminates considered consist of n fiber reinforced plies, each with a thickness t_i, $i=1,n$, leading to a total thickness $h=\sum_{i=1,n} t_i$ and ply volume fraction $c_i = t_i / h$ such that $\sum_{i=1,n} c_i = 1$. Two coordinates systems are considered (Fig. 1); one is local, which coincides with the material principal axes of each ply, and one is overall, which is selected such that the x_1x_2-plane coincides with mid-plane of the laminate, and the x_3-axis is in the thickness direction. The local coordinate system is denoted $\bar{x}_k$, $k=1,2,3$, such that the $\bar{x}_3$-axis coincides with the longitudinal direction of the fibers, and $\bar{x}_1\bar{x}_2$ is transverse plane of the fibrous lamina. The fiber orientation is defined in terms of the angle φ_i, $i=1,n$, enclosed by the local $\bar{x}_3$-axis and the overall x_1-axis (Fig. 1). The overall loads consist of membrane forces $\mathcal{N}=[\mathcal{N}_1,\mathcal{N}_2,\mathcal{N}_{12}]$, bending moments $\mathcal{M}=[\mathcal{M}_1,\mathcal{M}_2,\mathcal{M}_{12}]$, Fig. 1, and a piecewise uniform change of temperature θ_i, $i=1,n$, across the laminate thickness.

Each ply is a unidirectional, fibrous composite reinforced with piezoelectric filaments. Volume fractions of the fiber (*f*) and matrix (*m*) are denoted by v_f, v_m, such that $v_f + v_m = 1$. With regard to thermoelastic behavior, the matrix is assumed to be isotropic while the fiber is transversely isotropic. Let E, G, ν, and α denote Young's modulus, shear modulus, Poission's ratio, and coefficient of thermal expansion, respectively. Thermoelastic properties of the matrix are then identified as E_m, ν_m (or $G_m = 0.5E_m/(1+\nu_m)$), and α_m. Properties of the fiber related to deformations in longitudinal planes are identified as E_f^l, G_f^l, ν_f^l, α_f^l, and those related to deformations in the transverse plane are identified as E_f^t, ν_f^t (or $G_f^t = 0.5E_f^t/(1+\nu_f^t)$), and α_f^t.

Only the fiber is assumed to possess piezo/pyroelectric characteristics (Bahei-El-Din and Micheal, [32]). The direct electrical response is defined in terms of the permittivity constants, $\kappa_{11} = \kappa_{22}$ in the transverse plane, and κ_{33} in the longitudinal direction. Two sets of properties define the electrically-coupled response, one for electromechanical, and one for thermoelectric. The latter is given in terms of the pyroelectric constants $q_{11} = q_{22}$ and q_{33}. The electromechanical coupling can be defined for transversely isotropic fibers in terms of three piezoelectric constants, d_{31}, d_{33}, and d_{15} [32].

3. INTERRELATIONS BETWEEN MULTIPLE SCALES

The proposed multiscale model for fibrous laminates considers an idealized microstructure of a fibrous ply and the interaction between the plies caused by mutual constraints. The idealized local stresses and strains within the ply are assumed to be piecewise uniform, and the ply overall stresses and strains are found as averages. In this section, the relations between the phase stress

and strain fields within the microstructure of a ply and the overall ply stresses and strains are summarized.

3.1 Micromechanics

Each unidirectional lamina is divided into Q phases, each has a volume fraction v_r, $r = 1, Q$, such that $\sum v_r = 1$. In averaging models of fibrous composites [35-38] where the local stresses and strains represent averages over the fiber and matrix subvolumes, the number of phases Q is two. In more refined models, which are based on analysis of a representative volume element, the fiber and matrix are divided into a number of subvolumes over which the local fields are idealized as piecewise uniform. Hence a phase, or a subvolume, may belong to the fiber or the matrix and $Q > 2$. In any case, the lamina overall stresses $\bar{\boldsymbol{\sigma}}$ and strains $\bar{\boldsymbol{\varepsilon}}$, referred to the material principal axes $\bar{x}_k$, $k = 1, 2, 3$, are expressed as volume averages of their local counterparts, $\boldsymbol{\sigma}_r$ and $\boldsymbol{\varepsilon}_r$, by

$$\bar{\boldsymbol{\sigma}} = \sum_{r=1,Q} v_r \boldsymbol{\sigma}_r , \quad \bar{\boldsymbol{\varepsilon}} = \sum_{r=1,Q} v_r \boldsymbol{\varepsilon}_r . \tag{1}$$

Constitutive behavior of the phases is expressed as the sum of the elastic response caused by mechanical loads and the response due to other ‘eigen’ effects, e.g. thermal, piezoelectric, etc., which cannot be removed by mechanical unloading. Hence,

$$\boldsymbol{\sigma}_r = \boldsymbol{L}_r \boldsymbol{\varepsilon}_r + \boldsymbol{\lambda}_r , \quad \boldsymbol{\varepsilon}_r = \boldsymbol{M}_r \boldsymbol{\sigma}_r + \boldsymbol{\mu}_r , \qquad r = 1, Q , \tag{2}$$

where $\boldsymbol{L}_r$, $\boldsymbol{M}_r = \boldsymbol{L}_r^{-1}$ are elastic stiffness and compliance [32], and $\boldsymbol{\lambda}_r$, $\boldsymbol{\mu}_r = -\boldsymbol{M}_r \boldsymbol{\lambda}_r$ are eigen stress and strain.

Similarly, constitutive behavior of a fibrous composite lamina can be written in the material principal axes, $\bar{x}_k$, as follows

$$\bar{\boldsymbol{\sigma}} = \bar{\boldsymbol{L}}\bar{\boldsymbol{\varepsilon}} + \bar{\boldsymbol{\lambda}}\,, \quad \bar{\boldsymbol{\varepsilon}} = \bar{\boldsymbol{M}}\bar{\boldsymbol{\sigma}} + \bar{\boldsymbol{\mu}}\,. \tag{3}$$

The lamina overall stiffness and compliance are given in terms of their phase counterparts by [35]

$$\bar{\boldsymbol{L}} = \sum_{r=1,Q} v_r \boldsymbol{L}_r \boldsymbol{A}_r\,, \quad \bar{\boldsymbol{M}} = \sum_{r=1,Q} v_r \boldsymbol{M}_r \boldsymbol{B}_r\,, \tag{4}$$

where $\boldsymbol{A}_r$, $\boldsymbol{B}_r$ are strain and stress concentration factors, such that

$$\boldsymbol{\varepsilon}_r = \boldsymbol{A}_r\bar{\boldsymbol{\varepsilon}}\,, \quad \boldsymbol{\sigma}_r = \boldsymbol{B}_r\bar{\boldsymbol{\sigma}}\,. \tag{5}$$

Micromechanical models which have been developed to generate the strain and stress concentration factors fall into one of two categories, averaging models and periodic array models. While averaging models offer closed forms for the concentration factors, periodic array model center on analysis of a unit cell, which provides the factors computationally [19].

The lamina eigen strains and stresses are given in terms of their phase counterparts by [39]

$$\bar{\boldsymbol{\lambda}} = \sum_{r=1,Q} v_r \boldsymbol{A}_r^T \boldsymbol{\lambda}_r\,, \quad \bar{\boldsymbol{\mu}} = \sum_{r=1,Q} v_r \boldsymbol{B}_r^T \boldsymbol{\mu}_r\,. \tag{6}$$

Finally, the phase strains and stresses are given by superposition of the overall effect, Eq. (5), and the local effects caused by the eigen strains and stresses [39];

$$\boldsymbol{\varepsilon}_r = \boldsymbol{A}_r\bar{\boldsymbol{\varepsilon}} + \sum_{s=1,Q} \boldsymbol{D}_{rs}\boldsymbol{\mu}_s\,, \quad \boldsymbol{\sigma}_r = \boldsymbol{B}_r\bar{\boldsymbol{\sigma}} + \sum_{s=1,Q} \boldsymbol{F}_{rs}\boldsymbol{\lambda}_s\,, \quad r = 1,Q\,. \tag{7}$$

Here, $\boldsymbol{D}_{rs}$ and $\boldsymbol{F}_{rs}$ are strain and stress influence functions. They too can be found in closed form for averaging models, but are available only numerically for periodic array models [40].

The concentration factors and the influence functions follow the identities [40],

$$\sum_{s=1,Q} c_r \boldsymbol{A}_r = \boldsymbol{I}\,, \quad \sum_{s=1,Q} c_r \boldsymbol{B}_r = \boldsymbol{I}\,, \tag{8}$$

$$\sum_{s=1,Q} c_r \boldsymbol{F}_{rs} = \boldsymbol{0}\,, \quad \sum_{s=1,Q} c_r \boldsymbol{F}_{rs} = \boldsymbol{0}\,, \quad r = 1,Q\,. \tag{9}$$

3.2 Laminates

Having related the phase stresses to the lamina stresses, we now direct our attention to describing the latter in terms of the laminate loads, namely membrane forces $\mathcal{N}=[\mathcal{N}_1,\mathcal{N}_2,\mathcal{N}_{12}]$, and bending moments $\mathcal{M}=[\mathcal{M}_1,\mathcal{M}_2,\mathcal{M}_{12}]$. As a first step, the lamina in-plane stresses and strains, denoted $\hat{\bar{\boldsymbol{\sigma}}}=[\bar{\sigma}_{11},\bar{\sigma}_{22},\bar{\sigma}_{12}]$ and $\hat{\bar{\boldsymbol{\varepsilon}}}=[\bar{\varepsilon}_{11},\bar{\varepsilon}_{22},2\bar{\varepsilon}_{12}]$, are extracted from the full (6x1) vectors, and described in the overall coordinate system of the laminate x_j, $j=1,2,3$, Fig. 1:

$$\hat{\bar{\boldsymbol{\sigma}}}=\hat{\boldsymbol{I}}\bar{\boldsymbol{\sigma}},\quad \hat{\bar{\boldsymbol{\varepsilon}}}=\hat{\boldsymbol{I}}\bar{\boldsymbol{\varepsilon}},\quad \hat{\bar{\boldsymbol{\sigma}}}=\boldsymbol{R}\hat{\boldsymbol{\sigma}},\quad \hat{\bar{\boldsymbol{\varepsilon}}}=\boldsymbol{N}\hat{\boldsymbol{\varepsilon}}, \tag{10}$$

$$\hat{\boldsymbol{I}}=\begin{bmatrix}1&0&0&0&0&0\\0&0&1&0&0&0\\0&0&0&0&1&0\end{bmatrix},\quad \boldsymbol{R}^T=\boldsymbol{N}^{-1}=\begin{bmatrix}\cos^2\varphi&\sin^2\varphi&-0.5\sin 2\varphi\\ \sin^2\varphi&\cos^2\varphi&0.5\sin 2\varphi\\ \sin 2\varphi&-\sin 2\varphi&\cos 2\varphi\end{bmatrix}. \tag{11}$$

In analogy with eq. (3), the in-plane stresses and strains are directly related by a stiffness matrix and compliance matrix. These are denoted, respectively, by $\hat{\bar{\boldsymbol{L}}}$, $\hat{\bar{\boldsymbol{M}}}=\hat{\bar{\boldsymbol{L}}}^{-1}$ in the material principal axes of the ply, $\bar{x}_k$, and $\hat{\boldsymbol{L}}$, $\hat{\boldsymbol{M}}=\hat{\boldsymbol{L}}^{-1}$ in the overall axes, x_j, Fig. 1. The form of these matrices together with their coordinate transformation can be found in Bahei-El-Din and Micheal [32].

In general, the stresses and strains vary point wise across the laminate thickness, and the lamina stresses and strains in eq. (10) represent averages over the ply thickness. Hence,

$$\hat{\boldsymbol{\sigma}}_i=\frac{1}{t_i}\int_{z_i-t_i/2}^{z_i+t_i/2}\hat{\boldsymbol{\sigma}}(z)dz,\quad \hat{\boldsymbol{\varepsilon}}_i=\frac{1}{t_i}\int_{z_i-t_i/2}^{z_i+t_i/2}\hat{\boldsymbol{\varepsilon}}(z)dz, \tag{12}$$

where $z\equiv x_3$ is Cartesian coordinate in direction perpendicular to the laminated plate (Fig. 1), with the origin located on the mid-plane of the laminate, and z_i is the x_3 coordinate of the mid-plane of the lamina.

The applied membrane forces and bending moments are expressed as resultants of the lamina stresses;

$$\mathcal{N} = \int_{-h/2}^{h/2} \hat{\boldsymbol{\sigma}}(z)dz = \sum_{i=1,n}\left(\int_{z_i - t_i/2}^{z_i + t_i/2} \hat{\boldsymbol{\sigma}}(z)dz\right) = \sum_{i=1,n} t_i \hat{\boldsymbol{\sigma}}_i \,, \tag{13}$$

$$\mathcal{M} = \int_{-h/2}^{h/2} z\hat{\boldsymbol{\sigma}}(z)dz = \sum_{i=1,n}\left(\int_{z_i - t_i/2}^{z_i + t_i/2} z\hat{\boldsymbol{\sigma}}(z)dz\right). \tag{14}$$

Considering thin laminates, transverse shear deformations are negligible, and the in-plane strains $\hat{\boldsymbol{\varepsilon}}(z) = [\varepsilon_{11}, \varepsilon_{22}, 2\varepsilon_{12}]$ are assumed to vary linearly across the thickness with the z coordinate. Hence,

$$\hat{\boldsymbol{\varepsilon}}(z) = \boldsymbol{\varepsilon}_o + z\boldsymbol{\kappa}, \tag{15}$$

where $\boldsymbol{\varepsilon}_o = [\varepsilon^o_{11}, \varepsilon^o_{22}, 2\varepsilon^o_{12}]$ is the strain at mid-plane of the laminate, and $\boldsymbol{\kappa} = [\kappa_1, \kappa_2, \kappa_{12}]$ is the curvature with respect to the mid-plane. Considering eigen stresses and strains that may be generated in the individual plies, the mid-plane strain and curvature of the laminate are related to the applied loads according to the following modified relations [20]:

$$\boldsymbol{\varepsilon}_o = \mathcal{A}'\mathcal{N} + \mathcal{B}'\mathcal{M} + \boldsymbol{f}' \,, \quad \boldsymbol{\kappa} = \mathcal{C}'\mathcal{N} + \mathcal{D}'\mathcal{M} + \boldsymbol{g}' \,. \tag{16}$$

The coefficient matrices in the first two terms of eq. (16) are a function of the elastic properties of the laminas, their volume fractions and laminate layup;

$$\mathcal{A}' = (\boldsymbol{I} - \mathcal{B}'\mathcal{B})\mathcal{A}^{-1} \,, \quad \mathcal{B}' = -\mathcal{A}^{-1}\mathcal{B}\mathcal{D}' \,, \quad \mathcal{C}' = -\mathcal{D}'\mathcal{B}\mathcal{A}^{-1} \,, \quad \mathcal{D}' = [\mathcal{D} - \mathcal{B}\mathcal{A}^{-1}\mathcal{B}]^{-1}, \tag{17}$$

$$\mathcal{A} = \sum_{i=1,n} t_i \hat{\boldsymbol{L}}_i \,, \quad \mathcal{B} = \sum_{i=1,n} (t_i z_i)\, \hat{\boldsymbol{L}}_i \,, \quad \mathcal{D} = \sum_{i=1,n} t_i \left(\frac{1}{12} t_i^2 + z_i^2\right) \hat{\boldsymbol{L}}_i \,. \tag{18}$$

The eigen strain $\boldsymbol{f}'$ and curvature $\boldsymbol{g}'$ are discussed in Section 3.3 where the treatment of eigen fields on all length scales is presented.

To complete the formulation for laminates, the ply stresses are found in analogy of eq. (7) as the superposition of the stress caused by the overall membrane forces and bending moments, and those caused by the eigenstresses [20];

$$\hat{\boldsymbol{\sigma}}_i(z_i) = \boldsymbol{P}_i\mathcal{N} + \boldsymbol{Q}_i\mathcal{M} + \sum_{j=1,n} \boldsymbol{U}_{ij}\hat{\boldsymbol{\lambda}}_j \,, \tag{19}$$

The coefficient matrices, $\boldsymbol{P}_i$, $\boldsymbol{Q}_i$ denote stress distribution factors, and $\boldsymbol{U}_{ij}$ denotes stress transformation influence functions. They vary point wise along the laminate thickness, and are a function of elastic moduli and volume fractions of the laminas, and the laminate layup;

$$\boldsymbol{P}_i = \hat{\boldsymbol{L}}_i\left(\mathcal{A}' + z_i\mathcal{C}'\right), \quad \boldsymbol{Q}_i = \hat{\boldsymbol{L}}_i\left(\mathcal{B}' + z_i\mathcal{D}'\right), \tag{20}$$

$$\boldsymbol{U}_{ij} = \delta_{ij}\boldsymbol{I} - t_j\boldsymbol{P}_i - \left(t_j z_j\right)\boldsymbol{Q}_i \,. \tag{21}$$

Here too, discussion of the lamina eigenstress $\hat{\boldsymbol{\lambda}}_j$ will be included in Section 3.3. Finally, we note the following identities for the ply distribution factors and influence function, which are derived from the equilibrium of the lamina forces [20]:

$$\sum_{i=1,n} t_i\boldsymbol{P}_i = \boldsymbol{I}, \quad \sum_{i=1,n}\left(t_i z_i\right)\boldsymbol{P}_i = \boldsymbol{0}, \tag{22}$$

$$\sum_{i=1,n} t_i\boldsymbol{Q}_i = \boldsymbol{0}, \quad \sum_{i=1,n}\left(t_i z_i\right)\boldsymbol{Q}_i = \boldsymbol{I}. \tag{23}$$

4. EIGN STRESSES AND STRAINS

The eigen stresses and strains are auxiliary fields which are present in addition to those caused by mechanical loads and cannot be removed by unloading. Their effect on local and overall fields is considered as a superposition on the mechanical effects as indicated in eqs. (2), (3), and (16) for the phases of a fibrous composite, for a lamina, and for the laminate, respectively. The phase eigen stresses and strains, $\boldsymbol{\lambda}_r$, $\boldsymbol{\mu}_r$, $r = 1,Q$, are related to their ply

counterparts, $\bar{\boldsymbol{\lambda}}$, $\bar{\boldsymbol{\mu}}$ by eq. (6) [39]. The latter lead to eigen deformations for the laminate, namely, eigenstrain $\boldsymbol{f}'$ for strains of the laminate mid-plane, and eigencurvature, $\boldsymbol{g}'$, eq. (16). These are found by Bahei-El-Din et al. [20] as

$$\boldsymbol{f}' = -\mathcal{B}'\boldsymbol{g} - \mathcal{A}'\boldsymbol{f}\,, \quad \boldsymbol{g}' = -\mathcal{C}'\boldsymbol{f} - \mathcal{D}'\boldsymbol{g}\,, \tag{24}$$

$$\boldsymbol{f} = \sum_{i=1,n} t_i \hat{\boldsymbol{\lambda}}_i\,, \quad \boldsymbol{g} = \sum_{i=1,n} (t_i z_i)\hat{\boldsymbol{\lambda}}_i\,, \tag{25}$$

where $\hat{\boldsymbol{\lambda}}_i$ denotes the in-plane eigenstresses of the ply described in the overall coordinate system of the laminate (Fig. 1). They are related to the full eigenstress vector $\bar{\boldsymbol{\lambda}}_i$ described in the ply coordinate system by the stress reduction and transformation relations given in eq. (10). Accordingly, the entire eigen stress and strain fields at all length scales is defined as long as those available at the microscopic level in the fiber and matrix constituents, or their subdivisions, are described.

4.1 Thermo-Electro-Mechanical Coupling

Considering first electro-thermo-mechanical coupling effects, the eignstresses and eignstrains in phase or subvolume V_r subjected to electrical field $\boldsymbol{\mathcal{E}} = \left[\mathcal{E}_1, \mathcal{E}_2, \mathcal{E}_3\right]$ and/or thermal change θ can be expressed as [4, 8]

$$\boldsymbol{\lambda}_r = -\boldsymbol{e}_r^T\boldsymbol{\mathcal{E}} - \boldsymbol{L}_r\boldsymbol{\alpha}_r\theta\,, \quad \boldsymbol{\mu}_r = \boldsymbol{d}_r^T\boldsymbol{\mathcal{E}} + \boldsymbol{\alpha}_r\theta\,. \tag{26}$$

The coupling matrices $\boldsymbol{e}_r$ and $\boldsymbol{d}_r$ list the piezoelectric constants, $\boldsymbol{\alpha}_r$ lists the coefficients of thermal expansion. For transversely isotropic materials, they take the following form (Bahei-El-Din, [34])

$$\boldsymbol{d}^{\mathrm{T}}=\begin{bmatrix} 0 & 0 & d_{31} \\ 0 & 0 & d_{31} \\ 0 & 0 & d_{33} \\ 0 & d_{15} & 0 \\ d_{15} & 0 & 0 \\ 0 & 0 & 0 \end{bmatrix},\quad \boldsymbol{e}^{\mathrm{T}}=\begin{bmatrix} 0 & 0 & e_{31} \\ 0 & 0 & e_{31} \\ 0 & 0 & e_{33} \\ 0 & e_{15} & 0 \\ e_{15} & 0 & 0 \\ 0 & 0 & 0 \end{bmatrix},\quad \boldsymbol{\alpha}=\begin{Bmatrix} \alpha_T \\ \alpha_T \\ \alpha_L \\ 0 \\ 0 \\ 0 \end{Bmatrix}. \tag{27}$$

The piezoelectric constants are related by the elastic mechanical moduli,

$$e_{31}=2kd_{31}+\ell d_{33},\quad e_{33}=2\ell d_{31}+nd_{33},\quad e_{15}=pd_{15}, \tag{28}$$

where k,ℓ,m,n,p are Hill's elastic moduli [35].

For completeness, we list the electric displacement and field resulting from direct and coupling effects as follows:

$$\mathcal{D}=\boldsymbol{\kappa}_{\varepsilon}\mathcal{E}+\boldsymbol{e}\boldsymbol{\varepsilon}-\boldsymbol{q}\theta=\boldsymbol{\kappa}_{\sigma}\mathcal{E}+\boldsymbol{d}\boldsymbol{\sigma}-\boldsymbol{q}\theta, \tag{29}$$

$$\mathcal{E}=\boldsymbol{\kappa}_{\sigma}^{-1}\mathcal{D}-\boldsymbol{g}\boldsymbol{\sigma}+\boldsymbol{h}\theta, \tag{30}$$

where $\boldsymbol{q}$ is pyroelectric constant, $\boldsymbol{g}$ is voltage constant, $\boldsymbol{h}$ is thermo-electric coupling constant, and $\boldsymbol{\kappa}$ is the permittivity matrix, which can be measured at constant stress, $\boldsymbol{\kappa}_{\sigma}$, or at constant strain, $\boldsymbol{\kappa}_{\varepsilon}$. The following connections exist and can be readily verified [32],

$$\boldsymbol{g}=\boldsymbol{\kappa}_{\sigma}^{-1}\boldsymbol{d},\quad \boldsymbol{h}=\boldsymbol{\kappa}_{\sigma}^{-1}\boldsymbol{q}. \tag{31}$$

For a transversely isotropic material, the only nonzero constants are $\kappa_{11}=\kappa_{22}$ and κ_{33}. In this case, the voltage matrix $\boldsymbol{g}$ takes the same form as the piezoelectric constant $\boldsymbol{d}$, eq. (27). Hence, $g_{31}=d_{31}/\kappa_{33\sigma}$, $g_{33}=d_{33}/\kappa_{33\sigma}$, $g_{15}=d_{15}/\kappa_{11\sigma}$.

4.2 Damage

The treatment of damage follows the scheme developed by Bahei-El-Din et al. [27] in which auxiliary transformation fields are introduced to evacuate the stresses caused by the applied

loads. Let $\boldsymbol{\lambda}_s^{AUX}$ represent such fields, which are introduced in Ω subvolumes of a representative volume element of a unidirectional composite, where certain failure criteria are satisfied as described in the Appendix. These are yet unknown, but can be found from eq. $(7)_2$ by writing the stress components in subvolume V_s, $s=1,\Omega$, $\Omega \le Q$, the total number of subvolumes, and limiting the magnitude of the stresses to zero. Hence,

$$\boldsymbol{\sigma}_s = \boldsymbol{B}_s \bar{\boldsymbol{\sigma}} + \sum_{q=1,\Omega} \boldsymbol{F}_{sq} \boldsymbol{\lambda}_q^{AUX} = \boldsymbol{0}, \quad r=1,\Omega, \tag{32}$$

and the auxiliary field is thus determined.

Accordingly, the progression of damage is determined from elastic analysis of a lamina representative volume in the undamaged state, which is modified to reflect damage that can be inflicted at the total stresses arrived at so far. The overall load is usually applied in small increments in order to obtain a refined map of the damage progression. However, the damage state at a given load is independent of the number of load increments applied for a given loading path. On the other hand, the damage state predicted by this approach is a function of the loading path, which is the expected behavior.

5. MONITORING DEFORMATIONS

We now integrate the above formulation on the micromechanical, lamina, and laminate level to simulate monitoring of the overall and local deformations, including damage progression. The output of interest is the electric displacement $\mathcal{D}_r^i = [\mathcal{D}_1, \mathcal{D}_2, \mathcal{D}_3]_r^i$ in phase, or subvolume V_r, $1 \le r \le Q$, in lamina $1 \le i \le n$, caused by the laminate mechanical loads, $\mathcal{N} = [\mathcal{N}_1, \mathcal{N}_2, \mathcal{N}_{12}]$ and $\mathcal{M} = [\mathcal{M}_1, \mathcal{M}_2, \mathcal{M}_{12}]$, and lamina temperature change θ_i. Moreover, we assume that phase V_r is

subjected to electric field $\mathcal{E}_r^i = [\mathcal{E}_1, \mathcal{E}_2, \mathcal{E}_3]_r^i$, and that the lamina temperature is uniform and hence the phase is subjected to $\theta_r^i = \theta_i$.

The phase electric displacement $\mathcal{D}_r^i$ is given by eq. (29) as the sum of the direct electric contribution and the coupling effect, both electro-mechanical and thermo-electric. The electro-mechanical coupling term is a function of the phase stress $\boldsymbol{\sigma}_r^i$, which can be substituted in terms of the laminate mechanical loads, $\mathcal{N}$, $\mathcal{M}$, if eqs. (7) and (19) are utilized. In doing this exercise, eq. (10) is utilized to extract the in-plane stresses from the lamina full stress, and transform the former between the lamina principle axes and the laminate overall axes. Hence,

$$\mathcal{D}_r^i = \boldsymbol{\kappa}_{\sigma r}{}^i \mathcal{E}_r^i + \boldsymbol{d}_r^i \left[\boldsymbol{B}_r^i \hat{\boldsymbol{I}}^T \boldsymbol{R}_i \left(\boldsymbol{P}_i \mathcal{N} + \boldsymbol{Q}_i \mathcal{M} + \sum_{j=1,n} \boldsymbol{U}_{ij} \hat{\boldsymbol{\lambda}}_j \right) + \sum_{s=1,Q} \boldsymbol{F}_{rs}^i \boldsymbol{\lambda}_s^i \right] - \boldsymbol{q}_r^i \theta_i \,. \tag{33}$$

The entire collection of phase eigen stresses $\boldsymbol{\lambda}_q^i$, $1 \le q \le Q$, $1 \le i \le n$, contribute to the electric displacement in a given phase or subvolume V_r twice; through the stress due to constraints caused by the fully bonded laminas, and through the stress caused by micromechanical constraints within a lamina. In eq. (33), these effects are represented by the first and second terms in the brackets, respectively. Utilizing eq. (26), and assuming the presence of a set of auxiliary eigen stress $\boldsymbol{\lambda}_{\eta,j}^{AUX}$ (Section 4.2) in subvolumes V_η, $\eta = 1, \Omega_j$, $\Omega_j \le Q$, $1 \le j \le n$, eq. (33) can be expanded as

$$\begin{aligned} \mathcal{D}_r^i = {} & \boldsymbol{\kappa}_{\sigma r}{}^i \mathcal{E}_r^i - \boldsymbol{q}_r^i \theta_i \\ & + \boldsymbol{d}_r^i \left[\boldsymbol{B}_r^i \hat{\boldsymbol{I}}^T \boldsymbol{R}_i \left(\boldsymbol{P}_i \mathcal{N} + \boldsymbol{Q}_i \mathcal{M} - \sum_{j=1,n} \boldsymbol{U}_{ij} \boldsymbol{N}_j^T \hat{\boldsymbol{I}} \left\{ \sum_{q=1,Q} v_q^j \boldsymbol{A}_q^{jT} \left(\boldsymbol{e}_q^{jT} \mathcal{E}_q^j + \boldsymbol{L}_q^j \boldsymbol{\alpha}_q^j \theta_q \right) + \sum_{\eta=1,\Omega_j} v_\eta^j \boldsymbol{A}_\eta^{jT} \boldsymbol{\lambda}_{\eta,j}^{AUX} \right\} \right) \right. \\ & \left. - \left(\sum_{s=1,Q} \boldsymbol{F}_{rs}^i \left(\boldsymbol{e}_s^{iT} \mathcal{E}_s^i + \boldsymbol{L}_s^i \boldsymbol{\alpha}_s^i \theta_i \right) + \sum_{\eta=1,\Omega_i} \boldsymbol{F}_{r\eta}^i \boldsymbol{\lambda}_{\eta,i}^{AUX} \right) \right]. \end{aligned} \tag{34}$$

The first two terms represent the direct electric effect and the pyroelectric coupling effect, respectively. The last term represents the electromechanical coupling effect, with contributions from all stress components that are present in piezoelectric phases or subvolumes. These include stresses caused by overall mechanical loads applied to the laminate and by eigenstresses found in the phases. The latter are either generated due change of temperature and/or caused by an electric field, or introduced to simulate damage. The last term in eq. (34) represents the self induced effects caused in the lamina where subvolume V_r resides. The cross effect among the laminas is described by the term within the parenthesis in the second term of eq. (34)

In the absence of the laminate mechanical loads, $\mathcal{N}$, $\mathcal{M}$, temperature change, θ_i, $1 \le i \le n$, and damage, and the introduction of a nonzero electric field in subvolume V_r of lamina i ($\mathcal{E}_q^k = 0$, $q \ne r$, $k \ne i$; $1 \le q \le Q$, $1 \le k \le n$) eq. (34) is reduced to

$$\mathcal{D}_r^i = \hat{\boldsymbol{\kappa}}_{\boldsymbol{\sigma}\,r}^{\;i}\, \mathcal{E}_r^i, \quad \hat{\boldsymbol{\kappa}}_{\boldsymbol{\sigma}\,r}^{\;i} = \boldsymbol{\kappa}_{\sigma r}^{\;i} - v_r^i \boldsymbol{d}_r^i \left[\boldsymbol{B}_r^i \hat{\boldsymbol{I}}^T \boldsymbol{R}_i \boldsymbol{U}_{ii} \boldsymbol{N}_i^T \hat{\boldsymbol{I}} \boldsymbol{A}_r^{iT} \boldsymbol{e}_r^{iT} + \boldsymbol{F}_{rr}^i \boldsymbol{e}_r^{iT} \right]. \tag{35}$$

Matrix $\hat{\boldsymbol{\kappa}}_{\boldsymbol{\sigma}\,r}^{\;i}$ defines the apparent permittivity of subvolume V_r in lamina i under constant stress. It is found by modifying the permittivity $\boldsymbol{\kappa}_\sigma$ by a certain magnitude, which depends on the deformation constraints found at the micromechanical and the laminate length scales.

If on the other hand the laminate mechanical loads are absent while a temperature change is applied uniformly to lamina i such that, $\theta_k = 0$, $k \ne i$, $1 \le i \le n$, the apparent pyroelectric constant for subvolume V_r in lamina i can be found from (34) as

$$\mathcal{D}_r^i = -\hat{\boldsymbol{q}}_r^i \theta_i, \quad \hat{\boldsymbol{q}}_r^i = \boldsymbol{q}_r^i - \boldsymbol{d}_r^i \left[\boldsymbol{B}_r^i \hat{\boldsymbol{I}}^T \boldsymbol{R}_i \boldsymbol{U}_{ii} \boldsymbol{N}_i^T \hat{\boldsymbol{I}} \sum_{q=1,Q} v_q^i \boldsymbol{A}_q^{iT} \boldsymbol{L}_q^i \boldsymbol{\alpha}_q^i + \sum_{s=1,Q} \boldsymbol{F}_{rs}^i \boldsymbol{L}_s^i \boldsymbol{\alpha}_s^i \right]. \tag{36}$$

Here too, the pyroelectric constant is modified to reflect the deformation constraints within the lamina and across the plies.

6. APPLICATIONS

In this section applications of the above methodology to fibrous laminates exhibiting damage under overall membrane loads and/or bending moments are presented. The laminates considered are comprised of a DY063 epoxy matrix reinforced with PZT-5A filaments at a volume fraction of 0.55. Tables 1 and 2 provide relevant properties of the fiber and matrix. Ultimate strength of the matrix is assumed at 31.72 MPa under tension and 115 MPa under compression, and the shear strength is assumed at 46.36 MPa [20]. In modeling each ply, both the periodic hexagonal array (PHA) model [41] and Mori-Tanaka averaging model [38] are considered. In the PHA model, the representative volume element is subdivided into a set of homogeneous elements, which belong to either the matrix or the fiber. One row of matrix subvolume, which is adjacent to the fiber is treated as an interface layers, with properties equal to those of the matrix, but with a coefficient of friction of 0.268 against sliding in either the longitudinal or the transverse directions (Bahei-El-Din et al., [20]).

The results presented include the overall response and readings of the electric displacement, $\mathcal{D}_3$, in the PZT fibers. Also, the apparent magnitude of the PZT fiber permittivity, κ_{33}, is reported. This is evaluated during the course of loading the laminates and evolution of damage by suspending the overall mechanical load at predetermined values and computing the corresponding electric displacement $\mathcal{D}_3^{Mech}$ in the fibers. An electrical field $\mathcal{E}_3 = 0.1\text{x}10^6$ V/m is then applied to the fibers in individual laminas and the updated electric displacement, $\mathcal{D}_3^{Mech+Electric}$, is computed. The aparaent permitivity in the PZT fibers is then found as (Eq. 30),

$$\kappa_{33} = \left(\mathcal{D}_3^{Mech+Electric} - \mathcal{D}_3^{Mech}\right) \Big/ \mathcal{E}_3 \,. \tag{37}$$

6.1 Damage under Membrane Load

In one application a symmetric, quasi-isotropic, $(0/\pm 45/90)_S$ laminate is subjected to overall axial load applied in the x_1-axis, which coincides with the 0^o fiber. Both the Mori-Tanaka averaging model and the PHA model are invoked. The computed stress-strain response is shown in Fig. 2. The plateau appearing at certain stress levels indicates failure at predetermined loads. In the PHA model, where local stresses are modeled as piecewise uniform, failure initiates in the off-axis plies at the fiber/matrix interface at overall stress of 60 MPa, and progresses in the matrix away from the interfaces as the load is increased. In the averaging model, on the other hand, the failure criteria involve average stresses and hence the onset of failure is overestimated at an overall stress of 80 MPa. Damage progression maps computed in the 45^o and 90^o plies using the PHA model are shown in Fig. 3.

The damage inflicted on the plies is reflected on the electric displacement, $\mathcal{D}_3$, computed in the PZT fiber (Fig. 4). The successive changes seen in the electric displacement at constant overall load are indicative of initiation of damage. The change in $\mathcal{D}_3$ relative to the applied overall stress past the onset of failure compared to the undamaged state is indicative of sustained damage.

Damage is also reflected on the magnitude of the PZT fiber apparent permittivity, κ_{33}. Figure 5 shows the change in permittivity of the 0^o and 45^o fibers as the laminate load is increased. As damage progresses, the constraints imposed on the fibers of a given ply are effectively relaxed, albeit at different degrees, and the permittivity increases relative to that found in the undamaged state and approaches the unconstrained, stand-alone magnitude. To reiterate how this is accomplished in the TFA approach described here, the effect of damage on the constituent

stresses is modeled by introducing auxiliary eigen stresses, which affect the electrical displacement and consequently the magnitude of the permittivity (eq. 37).

6.2 Damage under Bending Moment

In this application the $(0/\pm45/90)_s$ laminate utilized above is subjected to a bending moment $\mathcal{M}_1$ of -3.5 kN.m (Fig. 6) under a constant compressive membrane load $\mathcal{N}_1$, which causes an overall stress, σ_{11} of 30 MPa. The PHA model was invoked as well as damage.

Focusing on the strain at mid-plane of the laminate, ε_{11}^o, and curvature κ_1, Figs. 6 and 7 show how they are changing with the applied load and the initiation and progression of damage. Under pre-compression, $\sigma_{11} = -30$ MPa , which has not caused damage, the symmetric laminate, as expected, does not exhibit curvature, and the mid-plane strain is computed at $\varepsilon_{11}^o = -0.17\%$ (eq. 16). The latter remains constant as the bending moment $\mathcal{M}_1$ is applied and the laminate remains in the undamaged state. Under pre-compression and the quadratic failure criterion assumed for the matrix (Appendix), the lower (compression) side of the laminate is more susceptible to failure due to the bending moment described above. At $\mathcal{M}_1 = -1.6$ kN.m. matrix failure initiates in the lower $+45^o$ ply and the laminate is no longer symmetric. In this case, the neutral axis under bending effectively shifts upwards and the compressive strain at the mid-plane increases, while the curvature deviates from the undamaged profile as the bending moment is increased.

Figures 8 and 9 show change of the electric displacement, $\mathcal{D}_3$**,** in the PZT fibers of all plies. The closed symbols indicate the electric displacement at -3.5 kN.m. It is seen that the 0^o ply

located at the lower surface of the laminate see the largest change in electric displacement as the other, off-axis plies suffer from damage.

7. COMPARISON TO EXPERIMENTS

The multiscale scheme developed above was tested by comparing its predictions to experiments of fibrous laminates undergoing damage. The stress-strain response measured by Soden et al. [43] for a $(\pm 55)_2$, glass/epoxy composite laminate is simulated where the microstructure of the fibrous plies is modeled with the PHA idealization. The fiber is Silenka E-glass with longitudinal Young's modulus of 70 GPa, shear modulus of 30.8 GPa, and Poisson's ratio of 0.2 [44]. Longitudinal tensile strength of the fiber is 2.15 GPa. The matrix is MY750/HY917/DY063 epoxy, with Young's modulus of 3.35 GPa, shear modulus of 1.24 GPa, and Poisson's ratio of 0.35. The matrix tensile strength for the bulk epoxy material is 80 MPa, and shear strength is 70 MPa [44]. The fiber volume fraction is 0.6.

The composite laminate specimen reported by Soden et al. [43] is a tube subject to axial load and internal pressure. The fiber orientation for the $(\pm 55)_2$ is measured with respect to the tube circumference. The overall strains were measured by strain gages mounted to the surface of the tubular specimen far from the grips. The results predicted are those reported for hoop/axial stress ratio of 2, and were found for a laminated plate of the same layup and subjected to biaxial stress. In the predictions found with the multiscale scheme, the PHA model was invoked. Matrix failure was determined with the failure envelope of eq. (40) given in the Appendix. The ultimate tensile stress of the matrix was taken as 100 MPa, which is slightly larger than that reported by Soden et al. [44] for the bulk matrix. This magnitude of the ultimate tensile strength provided a better match of the overall stress-strain response of the laminate and is considered an in-situ magnitude

of the matrix strength under tension. The ultimate shear strength of the matrix was accordingly enhanced to 87.5 MPa.

Interface failure was also modeled as described in the Appendix. The ultimate tensile strength at the interface is taken as 31.72 MPa, and the ultimate shear strength is taken as 46.36 MPa. These were determined by Bahei-El-Din et al. [20] for the same composite material considered here by correlating the responses of a unidirectional composite under transverse tension and longitudinal shear found by testing [43] and by the Mori-Tanaka model. The coefficients of friction corresponding to slip at the interface due to longitudinal shear and transverse shear are assumed equal at 0.268 [20].

Comparison of the measured and predicted response under hoop/axial stress ratio of 2 for the $(\pm 55)_2$, glass/epoxy laminate is given in Fig. 10. There is significant nonlinearlity in the measured axial stress-strain response, which is captured quite well with the multiscale model. Response of the composite laminate measured in the hoop direction is on the other hand much stiffer but also matched very well by the predicted results.

8. CONCLUSIONS

The work presented is an integrated, multiscale approach for modeling damage initiation and progression in composite structures reinforced with electrically active filaments, which involves interactive analysis of two length scales; macroscopic, and microscopic. This approach provides seamless integration of the mechanics at the two length scales, including piezoelectric and pyroelectric coupling effects, and damage under overall thermomechanical loads and an electric field applied to electroactive fibers. Damage is simulated by introducing local transformation fields to the undamaged composite to leave a stress state, which reflects the

damage criteria. The effect of local fields, which are unrelated to mechanical loading, for example those emerging from damage and electro-thermo-mechanical coupling in the reinforcing filaments is evaluated by a transformation field approach.

The merit of the proposed approach lies in modeling all these effects together under one scheme in a multiscale analysis. This is illustrated in several examples for fibrous laminates subjected to membrane and bending loads, where damage is signaled through readouts of electric displacements and effective permittivity. The model predictions for the stress-strain response of a fibrous laminate, which is exhibiting a significant nonlinear behavior due to damage compare well with the experimental results. This encourages, and indeed paves the way for multiscale analysis of composite structures under services loads, including structural health monitoring.

ACKNOWLEDGEMENTS

This work was partially supported by a grant from the European Office for Aerospace Research & Development and AFOSR, Award No. FA9550-11-1-0076.

APPENDIX – FAILURE CRITERIA OF A FIBROUS COMPOSITE

The failure criteria utilized in the present work are those described in Bahei-El-Din et al. [20] for averaging models, and in Bahei-El-Din [34] and Bahei-El-Din and Botrous [19] for periodic array models.

When averaging models are utilized in laminates, four average stress components may exist in constituents of the unidirectional plies, $\sigma_{11}^r, \sigma_{22}^r, \sigma_{33}^r, \sigma_{13}^r$, $r = f, m$ (Fig. 1). Failure under axial stress σ_{33}^r occurs when the stress magnitude equals the ultimate strength, which may assume different magnitudes under tension and compression. If these are denoted by σ_{uT}^r, σ_{uC}^r, $r = f, m$, the failure criterion is written as $\sigma_{33}^r = \sigma_{uT}^r$ if $\sigma_{33}^r > 0$, and $\left|\sigma_{33}^r\right| = \sigma_{uC}^r$ if $\sigma_{33}^r < 0$.

Under transverse normal stresses, matrix failure occurs by slip on planes parallel to the fiber when the resolved shear stress exceeds the ultimate shear strength of the matrix, τ_u^m. The slip direction in this case is transverse to the fibers. Considering frictional slip, failure criterion of the matrix in this case can be written as

$$\frac{1}{2}\left|\sigma_{11}^m - \sigma_{22}^m\right| + \frac{1}{2}\eta_T \left\langle \sigma_{11}^m + \sigma_{22}^m \right\rangle = \tau_u^m, \tag{38}$$

where η_T is coefficient of friction for matrix slip in the transverse direction, $\langle x \rangle = x$ if $x < 0$, and $\langle x \rangle = 0$ if $x \geq 0$. An entirely different failure mode that may occur in the matrix is transverse cracking under tensile stresses, or failure under compressive stresses. The limiting conditions in this case are $\sigma_{22}^m = \sigma_{uT}^m$ if $\sigma_{22}^m > 0$, and $\left|\sigma_{22}^m\right| = \sigma_{uC}^m$ if $\sigma_{22}^m < 0$, $r = f, m$.

Under longitudinal shear, matrix failure occurs by slip in the longitudinal direction on planes parallel to the fiber. Considering again frictional slip, the onset of failure is written as

$$\sigma_{13}^m + \eta_L \left\langle \sigma_{11}^m \right\rangle = \tau_u^m, \tag{39}$$

where η_L is coefficient of friction. Since ply strength is matrix dominated under transverse loads and shear stresses, no failure criteria are specified under these stress components for the fiber. These stresses will however vanish in the fiber when the matrix fails, and accordingly the ply stresses also vanish.

In periodic array models the fiber and matrix stress fields are modeled as piecewise uniform over small subvolumes. The matrix is isotropic and its failure is treated as a terminal state, beyond which the material cannot support any load [34]. Under a local stress applied to a matrix subvolume, an ellipsoidal failure envelope is assumed. Hence,

$$f = \frac{1}{\sigma_u{}^2}\left(\sigma_{11}^2+\sigma_{22}^2+\sigma_{33}^2-\sigma_{11}\sigma_{22}-\sigma_{22}\sigma_{33}-\sigma_{33}\sigma_{11}\right)+\frac{3}{\tau_u{}^2}\left(\sigma_{23}^2+\sigma_{31}^2+\sigma_{12}^2\right)-1.0\,, \tag{40}$$

where σ_u is ultimate normal stress, and τ_u and shear stresses.

Fiber/matrix interface elements are thin matrix subvolumes, which fail by peeling and/or sliding. The latter occurs along the fiber circular circumference or along the fiber longitudinal direction. Resolving the subvolume stresses found in the lamina Cartesian coordinates into radial stress, $\sigma_{\rho\rho}$, transverse shear stress, $\sigma_{\rho\Psi}$, and longitudinal shear stress, $\sigma_{\rho\mathfrak{z}}$, where ρ is radial direction from the center of the fiber, and Ψ, is angular direction (Bahei-El-Din, [34]), failure by peeling is characterized by $\sigma_{\rho\rho}=\sigma_u$. Sliding at the interface in the transverse plane is caused by the tangential traction component and is characterized by $\sigma_{\rho\Psi}+\upsilon\left\langle\sigma_{\rho\rho}\right\rangle=\tau_u$, where υ is coefficient of friction. Sliding in the longitudinal plane is determined by the equality $\sqrt{\sigma_{\rho\mathfrak{z}}{}^2+\sigma_{\rho\Psi}{}^2}+\upsilon\left\langle\sigma_{\rho\rho}\right\rangle=\tau_u$.

REFERENCES

1. Aboudi J. Micromechanical analysis of fully coupled electro-magneto-thermo-elastic multiphase composites. Smart Mater Struct 2001; 10: 867-877.
2. Berger H, Kari S, Gabbert U, Rodriguez-Ramos R, Guinovart R, Otero JA, Bravo-Castillero J. An analytical and numerical approach for calculating effective material coefficients of piezoelectric fiber composites. Int J Solids Struct 2005; 42: 5692-5714.
3. Challagulla KS, Georgiades AV. Micromechanical analysis of magneto-electro-thermo-elastic composite materials with applications to multilayered structures. Int J Eng Sci 2011; 49: 85-104.
4. Chen T. Micromechanical estimates of the overall thermoelectroelastic moduli of multiphase fibrous composites. . Int J Solids Struct 1994; 31(22): 3099-3111.
5. Hadjiloizi DA, Georgiades AV, Kalamkarov AL, Jothi S. Micromechanical modeling of piezo-magneto-thermo-elastic composite structures: Part I – Theory. Eur J Mech A-Solid 2013; 39: 298-312.
6. Hadjiloizi DA, Georgiades AV, Kalamkarov A L, Jothi S. Micromechanical Modeling of Piezo-Magneto-Thermo-Elastic Composite Structures: Part II – Applications. Eur J Mech A-Solid 2013; 39: 313-327.
7. Della CN, Shu D. On the performance of 1-3 piezoelectric composites with a passive and active matrix. Sensor Actuator A 2007; 140: 200-2060.
8. Kumar A, Chakraborty D. Effective properties of thermo-electro-mechanically coupled piezoelectric fiber reinforced composites. Mater Design 2009; 30(4): 1216-1222.
9. Sato Y, Okabe T, Higuchi R, Yoshioka K. Multiscale approach to predict crack initiation in unidirectional off-axis laminates. Adv Compos Mater 2014; 23: 461-475.

10. Ivančević D, Smojver I. Micromechanical failure modelling of composite materials using HFGMC. In: Proceedings of 11th World Congress on Computational Mechanics, WCCM 2014, 5th European Conference on Computational Mechanics, ECCM 2014 and 6th European Conference on Computational Fluid Dynamics, ECFD 2014. Barcelona, July, 2014. p. 3715-3726.
11. Spahn J, Andrae H, Kabel M, Mueller R, Linder C. Multiscale modeling of progressive damage in elasto-plastic composite materials. In: Proceedings of 11th World Congress on Computational Mechanics, WCCM 2014, 5th European Conference on Computational Mechanics, ECCM 2014 and 6th European Conference on Computational Fluid Dynamics, ECFD 2014. Barcelona, July, 2014. P. 3426-3437.
12. Liu PF, Chu JK, Hou SJ, Zheng JY. Micromechanical damage modelling and multiscale progressive failure analysis of composite pressure vessel. Comp Mater Sci 2012; 60: 137-148.
13. Li X, Guan Z, Liu L, Li Z. Composite multiscale failure criteria and damage evolution. Fuhe Cailiao Xuebao/Acta Materiae Compositae Sinica 2013; 30(2):152-158.
14. Daghia F, Ladevèze, P . A micro-meso numerical strategy for the simulation of the degradation of laminated composites. In: Proceedings of European Congress on Computational Methods in Applied Sciences and Engineering ECCOMAS 2012. Vienna, 2012. p. 961-971.
15. Daghia F, Ladevèze P . A Micro-Meso Computational Strategy for the Prediction of the Damage and Failure of Laminates. Compos Struct 2012; 94(12): 3644-3653.
16. Kurnatowski B, Matzenmiller A. Coupled two scale analysis of fiber reinforced composite structures with microscopic damage evolution. . Int J Solids Struct 2012; 49(18): 2404-2417.

17. Mao JZ, Sun XS, Ridha M, Tan VBC, Tay TE. A modelling approach across length scales for progressive failure analysis of woven composites. Appl Compos Mater 2013; 20(3): 213-231.
18. Zhang B, Yang Z, Wu Y, Sun H. Hierarchical multiscale modelling of failure in unidirectional fiber-reinforced plastic matrix composite. Mater Design 2010; 31(5): 2312-2318.
19. Bahei-El-Din YA, Botrous AG. Analysis of progressive fiber debonding in elastic laminates. Int J Solids Struct 2003; 40(25): 7035-7053.
20. Bahei-El-Din YA, Khire R, Hajela P. Multiscale transformation field analysis of progressive damage in fibrous laminates. International Journal for Multiscale Computational Engineering 2010; 8(1): 69-80.
21. Khire R, Hajela P, Bahei-El-Din Y. Handling uncertainty propagation in laminated composites through multiscale modelling of progressive failure. In: Proceedings of the 48th AIAA/ASME/ASCE/ AHS/ASC Structures, Structural Dynamics, and Materials Conference. Honolulu, Hawaii, April, 2007. p. 23-26.
22. Kaddour AS, Hinton MJ. Damage prediction in polymeric composites: Up-date of part (A) of the third world-wide failure exercise (WWFE-III). In: Proceedings of the 18th International Conference on Composite Materials. Jeju, Korea, August, 2011. p. 21-26.
23. Kaddour AS, Hinton MJ. Maturity of 3D failure criteria for fibre-reinforced composites: comparison between theories and experiments: Part B of WWFE-II. J Compos Mater 2013; 47(6–7): 925–966.
24. García IG, Mantič V, Graciani E. A model for the prediction of debond onset in spherical-particle-reinforced composites under tension: application of a coupled stress and energy criterion. Compos Sci Technol 2015; 106: 60-67.

25. Li J, Lee JD, Chong KP. Multiscale analysis of composite material reinforced by randomly-dispersed particles. International Journal of Smart and Nano Materials 2012; 3(1): 2-13.
26. Yang W, Pan Y, Pelegri AA. Multiscale modelling of matrix cracking coupled with interfacial debonding in random glass fiber composites based on volume elements. J Compos Mater 2013; 47(27): 3389-3399.
27. Bahei-El-Din YA, Rajendran AM, Zikry MA. A micromechanical model for damage progression in woven composite systems. Int J Solids Struct 2004; 41(9-10): 2307-2330.
28. Borkowski L, Chattopadhyay A. Multiscale model of woven ceramic matrix composites considering manufacturing induced damage. Compos Struct 2015; 126: 62-71.
29. Coradi A, Couégnat G, Martin E, Mahdi F. A multiscale damage model for the mechanical behavior of ceramic matrix composite materials. In: Proceedings of the 15th European Conference on Composite Materials ECCM 2012. Venice, 2012.
30. Valisetty R, Rajendran A, Grove D. Mesh effects in predictions of progressive damage in 3D woven composites. Computer Modelling in Engineering and Sciences 2010; 60(1): 41-71.
31. Visrolia A, Meo M. Multiscale damage modelling of 3D weave composite by asymptotic homogenization. Compos Struct 2013; 95: 105-113.
32. Bahei-El-Din YA , Micheal AG. Micromechanical modeling of multifunctional composites. In: Proceedings of the International Mechanical Engineering Congress & Exposition ASME 2012 IMechE. Huston, Texas, November, 2012. No. 89304.
33. Bahei-El-Din YA, Micheal AG. Multiscale Analysis of Multifunctional Composite Structures. In: Proceedings of the ASME 2013 International Mechanical Engineering Congress & Exposition. ASME 2013 IMECE. San Diego, California, November, 2013. No. 62427.

34. Bahei-El-Din YA. Modeling electromechanical coupling in woven composites exhibiting damage. Proceedings of IMechE, Part G: J Aerospace Eng 2009; 223(5): 485-495.
35. Hill R. Theory of mechanical properties of fiber-strengthened materials: I. Elastic behavior. J Mech Phys Solids 1964; 12: 199-212.
36. Hill R. Theory of mechanical properties of fiber-strengthened materials: III. Self-Consistent Model. J Mech Phys Solids 1965; 13: 189-198.
37. Hill R. A self-consistent mechanics of composite materials. J Mech Phys Solids 1965; 13: 213-222.
38. Mori T, Tanaka K. Average stress in matrix and average elastic energy of materials with misfitting inclusions. Acta Metall Mater 1973; 21: 571-574.
39. Dvorak J. Transformation field analysis of inelastic composite materials. P R Soc London 1992; A437: 311-327.
40. Dvorak GJ, Benveniste Y. On transformation strains and uniform fields in multiphase elastic media. P R Soc London 1992; A437: 291–310.
41. Dvorak GJ, Teply JL. Plasticity today: modeling, methods, and applications. In: Sawczuk A, Bianchi G, editors. W. Olszak Memorial. Amsterdam: Elsevier Science Publishers 1985. p 623-642.
42. Berlincourt D, Krueger HHA, Near C. Properties of MORGAN electro ceramic ceramics. www.morgan-electrocceramics.com 2009.
43. Soden PD, Hinton MJ, Kaddour AS. Biaxial test results for strength and deformation of a range of E-glass and carbon fibre reinforced composite laminates: failure exercise benchmark data. Compos Sci Technol 2002; 62: 1489-1514.

44. Soden PD, Hinton MJ, Kaddour AS. Lamina properties, lay-up configurations and loading conditions for a range of fibre-reinforced composite laminates. Compos Sci Technol 1998; 58: 1011-1022.

FIGURES

Table 1. Mechanical properties of fiber and matrix (Berlincourt et al. [42]; Bahei-El-Din [9]; Kumar and Chakraborty [8]).

Material	E (GPa)	ν	α (10^{-6} /^{o}C)
PZT-5A	60	0.34	2.3
DY063 Epoxy	3.35	0.35	2.4

Table 2. Piezo/pyroelectric properties of PZT-5A (Berlincourt et al. [42]; Bahei-El-Din [34]).

d_{31}	d_{33}	d_{51}	g_{31}	g_{33}	g_{15}	q_3
(10^{-12} m/V)			(10^{-3} V.m/N)			10^{-2} (C/m^2.^{o}C)
-171	347	584	11.4	24.8	38.2	0.06

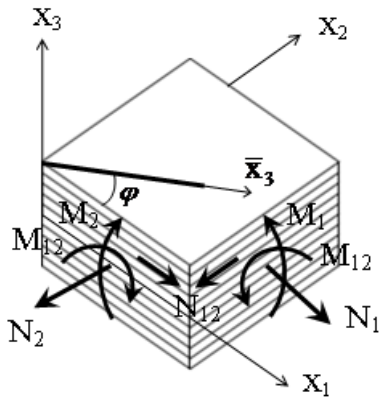

Fig. 1. Geometry and load of a fibrous laminate.

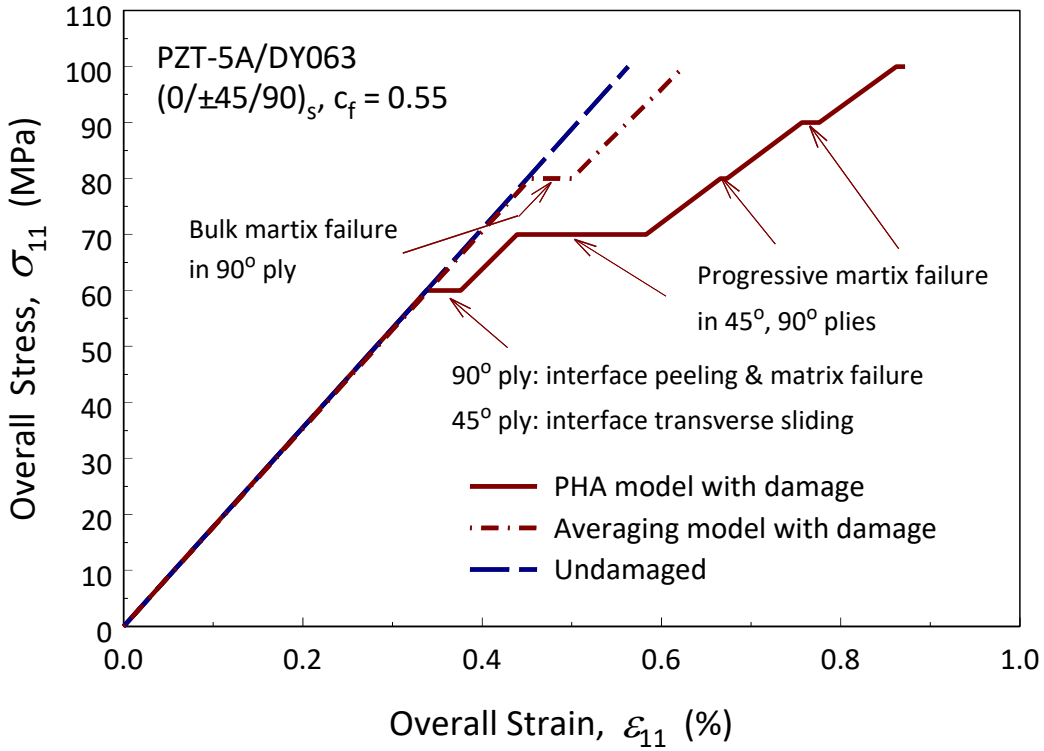

Fig. 2. Stress-strain response due to overall membrane load $\mathcal{N}_1$ (Fig. 1).

Y.A. Bahei-El-Din, A. Micheal, Mechanics of Materials, V.113, 2017

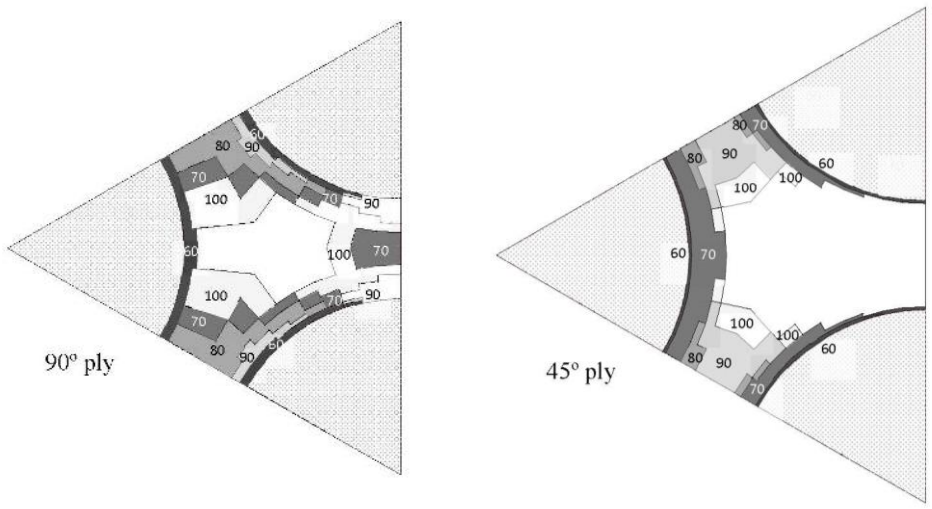

Fig. 3. Evolution of damage in off-axis plies due to overall membrane load $\mathcal{N}_1$ (Fig. 1).

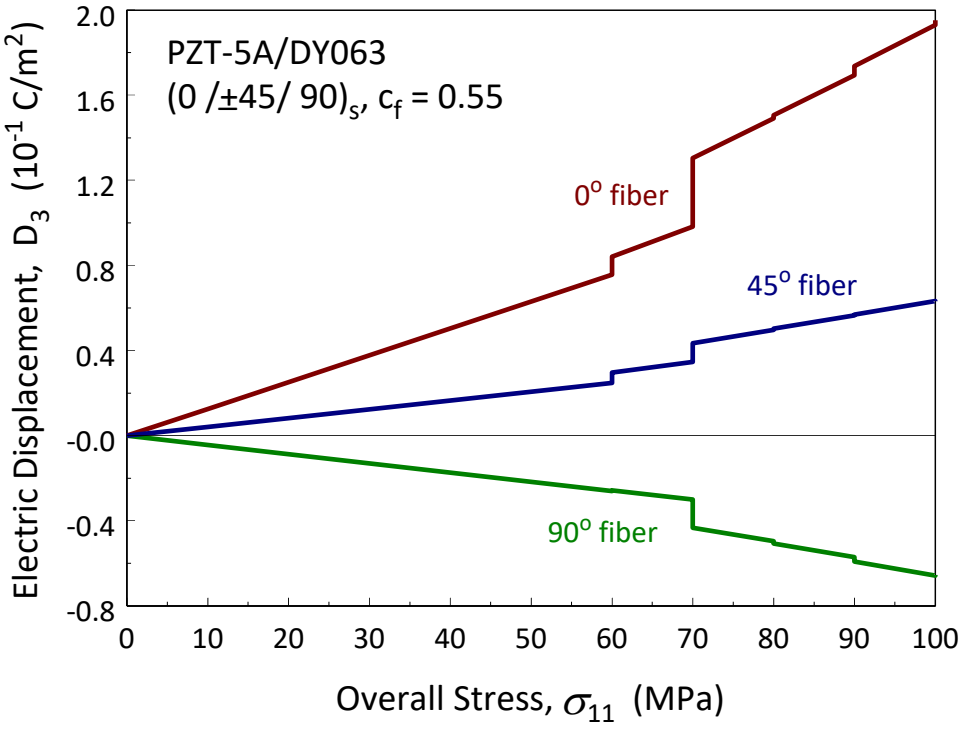

Fig. 4. Electric displacement due to overall membrane load $\mathcal{N}_1$ (Fig. 1).

Y.A. Bahei-El-Din, A. Micheal, Mechanics of Materials, V.113, 2017

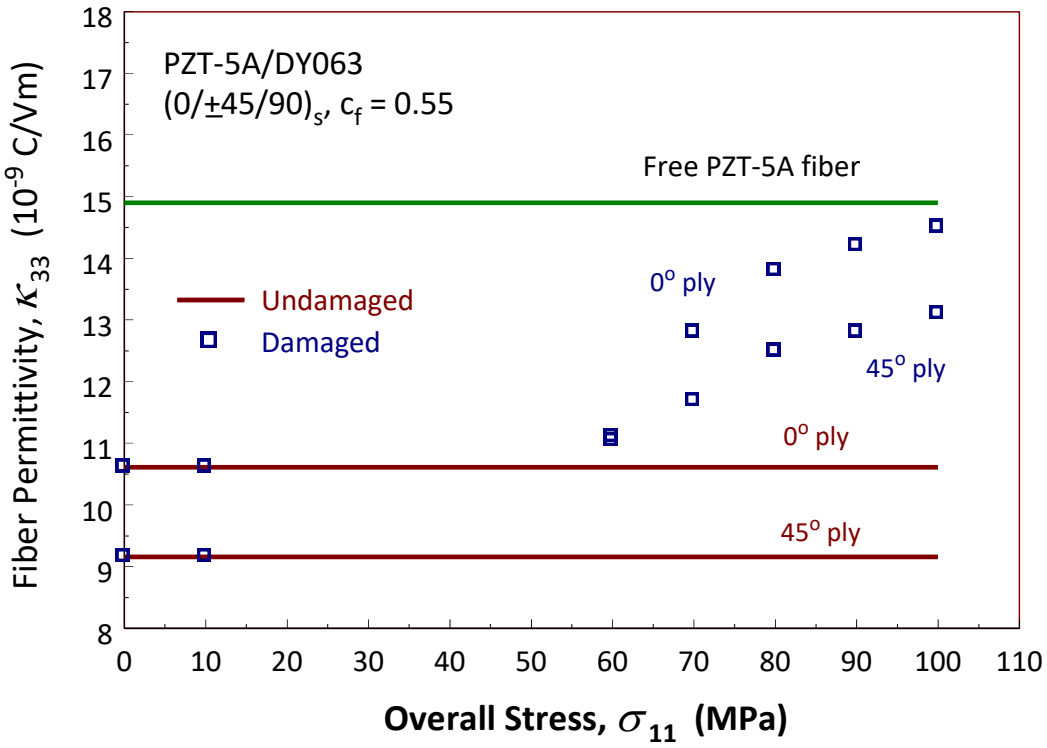

Fig. 5. Apparent permittivity due to overall membrane load $\mathcal{N}_1$ (Fig. 1).

Y.A. Bahei-El-Din, A. Micheal, Mechanics of Materials, V.113, 2017

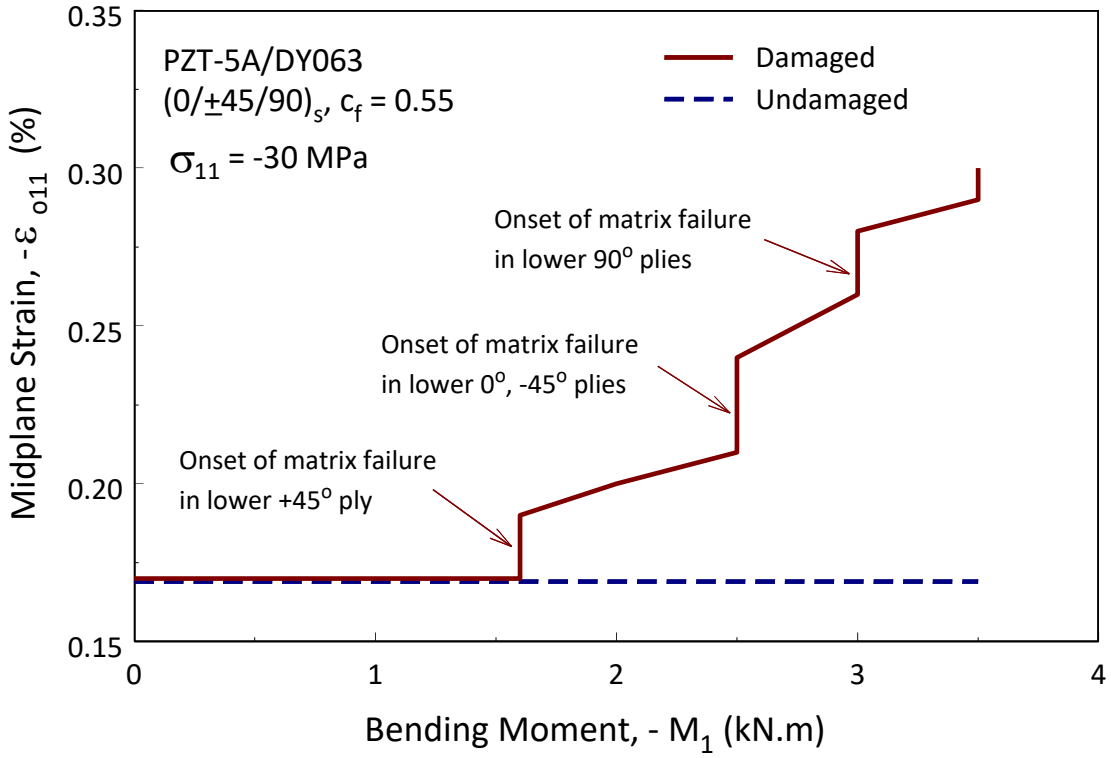

Fig. 6. Midplane strain due to bending moment $\mathcal{M}_1$ and sustained overall membrane load $\mathcal{N}_1$ (Fig. 1).

Y.A. Bahei-El-Din, A. Micheal, Mechanics of Materials, V.113, 2017

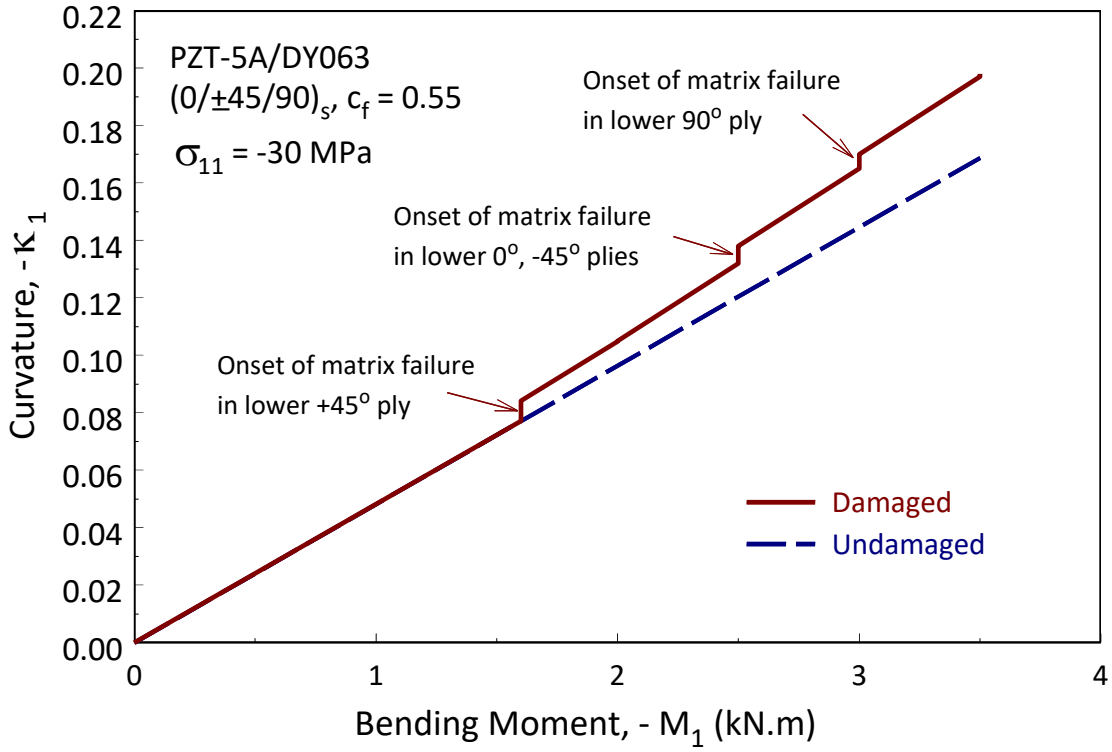

Fig. 7. Midplane curvature due to bending moment $\mathcal{M}_1$ and sustained overall membrane load $\mathcal{N}_1$ (Fig. 1).

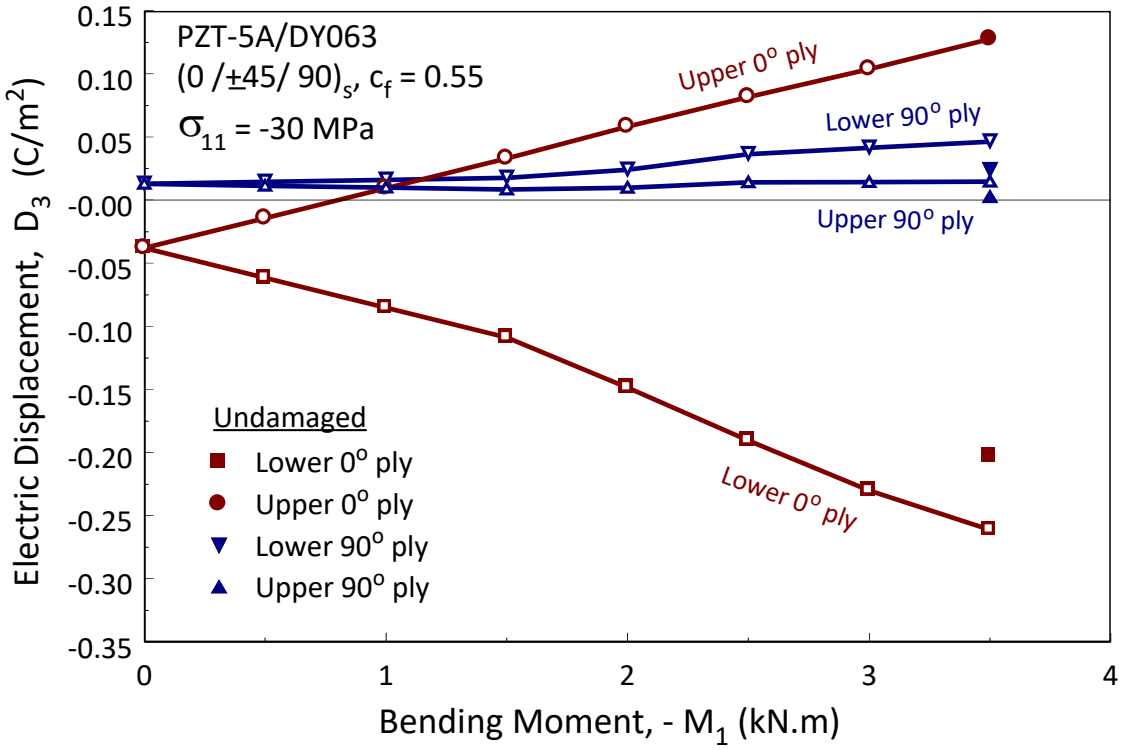

Fig. 8. Electric displacement in 0° and 90° plies due to bending moment $\mathcal{M}_1$ and sustained membrane load $\mathcal{N}_1$ (Fig. 1).

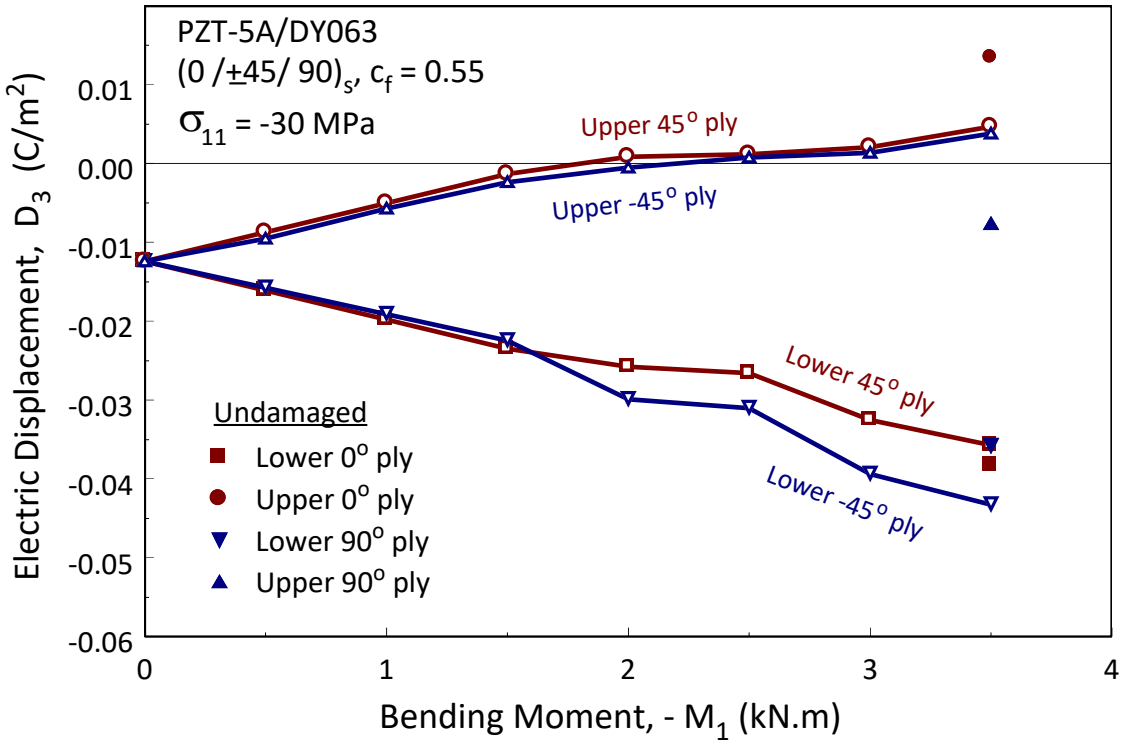

Fig. 9. Electric displacement in ±45° plies due to bending moment $\mathcal{M}_1$ and sustained membrane load $\mathcal{N}_1$ (Fig. 1).

Y.A. Bahei-El-Din, A. Micheal, Mechanics of Materials, V.113, 2017

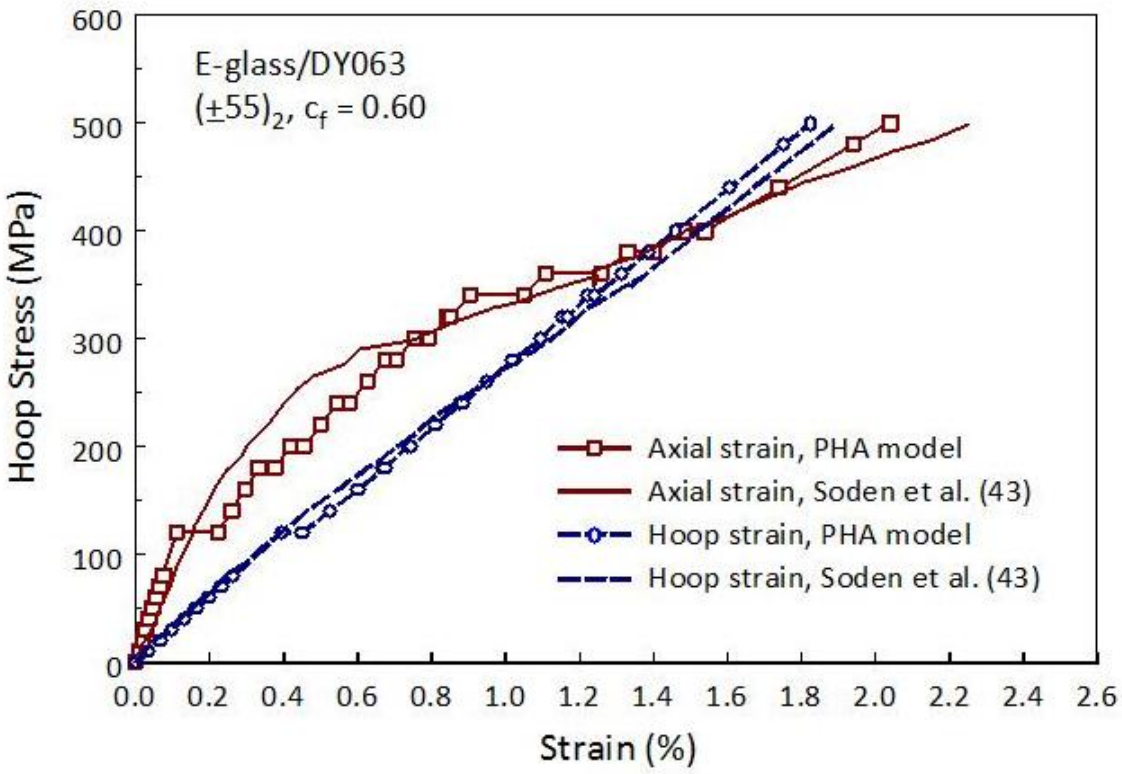

Fig. 10. Comparison of measured and predicted stress-strain response of a laminated composite tube subjected to hoop/axial stress ratio of 2.